
CONDITIONING GENERATIVE LATENT OPTIMIZATION TO SOLVE IMAGING INVERSE PROBLEMS

Thomas Braure

Commissariat à l’Énergie Atomique
2 Rue de la Piquetterie
91680 Bruyères-le-Châtel
France
thomas.braure@cea.fr

Kévin Ginsburger

Commissariat à l’Énergie Atomique
2 Rue de la Piquetterie
91680 Bruyères-le-Châtel
France
kginsburger@gmail.com

August 22, 2023

ABSTRACT

Computed Tomography (CT) is a prominent example of Imaging Inverse Problem (IIP), highlighting the unrivaled performances of data-driven methods in degraded measurements setups like sparse X-ray projections. Although a significant proportion of deep learning approaches benefit from large supervised datasets to directly map experimental measurements to medical scans, they cannot generalize to unknown acquisition setups. In contrast, fully unsupervised techniques, most notably using score-based generative models, have recently demonstrated similar or better performances compared to supervised approaches to solve IIPs while being flexible at test time regarding the imaging setup. However, their use cases are limited by two factors: (a) they need considerable amounts of training data to have good generalization properties and (b) they require a backward operator, like Filtered-Back-Projection in the case of CT, to condition the learned prior distribution of medical scans to experimental measurements. To overcome these issues, we propose an unsupervised conditional approach to the Generative Latent Optimization framework (cGLO), in which the parameters of a decoder network are initialized on an unsupervised dataset. The decoder is then used for reconstruction purposes, by performing Generative Latent Optimization with a loss function directly comparing simulated measurements from proposed reconstructions to experimental measurements. The resulting approach, tested on sparse-view CT using multiple training dataset sizes, demonstrates better reconstruction quality compared to state-of-the-art score-based strategies in most data regimes and shows an increasing performance advantage for smaller training datasets and reduced projection angles. Furthermore, cGLO does not require any backward operator and could expand use cases even to non-linear IIPs.

1 Introduction

Imaging Inverse Problems (IIPs) are a large and swiftly growing area of research. IIPs cover a large variety of applications, ranging from generic image processing topics such as denoising, super-resolution and deconvolution to more specific domains usually involving the characterization of a system of interest from indirect observations. In this latter case, the problem of reconstructing scans from medical imaging devices such as Computed Tomography (CT), Magnetic Resonance Imaging (MRI) and Positron Emission Tomography (PET) offers major challenges yet to be solved. Among those, CT reconstruction is a prime example of medical IIPs. The search of reduced ionizing radiations for patients has led to a sparsification of X-ray projection angles and/or a lowering of X-ray intensities resulting in noisier projection images. Using such degraded measurement setups, reconstructions obtained by conventional numerical methods, e.g. Filtered Back-Projection (FBP) [1, 125-147], are severely worsened.

Recent progresses have been made using deep learning approaches for CT reconstruction. However, a great part of these novel data-driven methods employ a supervised training setup [2, 3, 4, 5, 6, 7].

In supervised training pairs, ground truths consist of 3D volumetric scans reconstructed from conventional techniques such as the well-known FBP algorithm, using high-dose and densely sampled X-ray measurements. To each ground truth is associated a degraded set of measurements, obtained from sparsification and/or dose reduction from the original X-ray projections. Building such supervised datasets thus implies that a fixed physical model has been employed for all training pairs, which must be identical to the one used for inference. In other words, supervised reconstruction strategies need a new training whenever the acquisition process changes. This can be problematic when the viewing angles, X-ray spectrum or beam geometry vary. To circumvent this drawback, several unsupervised strategies have recently been introduced.

Current approaches dealing with ill-posed IIPs in an unsupervised way are mostly based on the use of generative models. As such, the infamous Generative Adversarial Networks (GANs) [8] are largely employed for unsupervised reconstruction tasks [9]. As a serious contender to GANs, Score-based Generative Models (SGMs) [10, 11] have gained a lot of attention in the past few years, as recent improvements lead to the generation of high-quality image samples without requiring a complex adversarial optimization. The basic principle of SGMs is to add noise of increasing intensity to data during the training process and learn to reverse this process in order to make a generative model from a sequence of trained denoisers. Using this general strategy, two types of approaches can be distinguished: Denoising Diffusion Probabilistic Models (DDPM) [11, 12, 13] and Score Matching methods [10, 14, 15]. In particular, Score Matching has been used to perform sparse CT reconstruction [16]. This method estimates the gradient of the prior log-likelihood, also called the score function, for each level of noise. In the continuous approach [15], the discrete sequence of noise levels is replaced by a continuum of distributions progressively diffusing data points into random noise following a Stochastic Differential Equation (SDE) describing a Markovian diffusion process. By estimating the score function with a time-dependent neural network, the reverse-time SDE is approximated. Using standard iterative sampling techniques then leads to generative capability.

Both GANs and SGMs are very efficient to learn unconditional prior distributions on slices of 3D reconstructed volumes. However, difficulties arise when a conditional sampling is needed to reconstruct slices from experimental X-ray projections. Various strategies have been proposed to deal with this conditional sampling issue.

GAN inversion approaches [9] start from a *trained and fixed* decoder, and aim at estimating the latent code corresponding to a given observation. The inversion process can be learning-based [17, 18], e.g. learning an encoder to inverse the decoder, optimization-based where the optimization problem is solved by finding the latent code minimizing the given objective function [19, 20], or both [21, 22, 23]. Other approaches using a parameterization of the latent space have been proposed, where the decoder and the encoder are jointly learned using an adversarial process [24, 25, 26, 27, 28, 29, 30]. Similar to GANs, conditional inference using SGMs is also quite unnatural. It is generally performed using a biased sampling of the posterior distribution to generate approximate samples from a stochastic process conditioned to experimental measurements. For instance, in the context of sparse CT reconstruction, conditioning a SGM to X-ray projections, as in [16], involves computing the FBP on experimental measurements filled with simulated measurements from the candidate reconstruction. To the best of our knowledge, this conditioned version of a SGM (cSGM) currently achieves state-of-the-art for unsupervised sparse CT reconstruction. However, cSGM is restricted to IIPs for which both a forward and an approximate pseudo-inverse operators are available. While such an inverse operator exists for single-material CT using for instance the FBP algorithm, this approach cannot be extended to other IIPs where pseudo-inverse operators are not defined, e.g. multi-material CT.

In addition to the conditional sampling issue, unsupervised generative models require large amounts of training data, which can be difficult to collect in the context of medical imaging. Furthermore, while these approaches have good generalization given infinite training data, in practice it is not clear how much is necessary.

On the other side of the data-consumption spectrum, Deep Image Prior (DIP) [31] has demonstrated that the structure of a deep convolutional network inherently captures a significant amount of low-level image statistics without any learning. In other words, it induces an implicit structural bias, i.e. a prior. DIP uses a randomly initialized U-Net like architecture [32], and a fixed input noise. The network weights can then be optimized to solve any ill-posed IIP with known forward model, such as inpainting or super-resolution. It has been shown that this IIP reparameterization, when optimized with gradient descent, hierarchically reconstructs from low to high frequencies, i.e. converging faster towards "natural images" than noise [33, 34]. The method has recently been adapted in [35] to solve low-dose and sparse CT reconstruction. While this strategy showed good results on use cases with missing or small datasets, it imposes a quite rough prior which cannot compete with the reconstruction performances of its data-driven counterparts in degraded measurement setups [16].

Considering, on one side, data-hungry generative models offering strong priors and limited to specific IIPs, and data-free methods providing weak priors on the other side, the question of a possible trade-off between these two extremes naturally arises.

As a way to alleviate this dilemma, this paper proposes a conditional version of the approach described as Generative Latent Optimization (GLO) [36]. The core idea of the original GLO technique is to use a decoder network and a set of *learnable* unit noise vectors, i.e. latent codes, where each code is associated to a single individual of the unsupervised training dataset. During training, the gradient is back-propagated both on the weights of the decoder and on the latent codes. In this GLO framework, the manifold defined by the latent codes is not parameterized. A direct consequence is that it is not trivial to sample from it. Decent generated samples can be produced when evaluating the decoder on linear combinations of latent codes or when sampling from a single full-covariance Gaussian fitted to the latent codes distribution. While these generations do not suffer from mode collapse, they are outperformed by GANs except when trained on small datasets. The vast majority of articles building on GLO are focused on improving its generative characteristics [37, 38, 39].

This paper differs from these recent works and from standard GAN inversion techniques which focus on parameterizing the manifold entailed by the latent codes. Similar to DIP, our conditioned version of GLO (cGLO) exploits the inherent structural prior induced by the convolutional network of the decoder. However, contrary to DIP, cGLO can benefit from an unsupervised training dataset of any size to initialize its decoder weights, resulting in greatly improved reconstruction results. The higher the quantity of training data for initialization is used, the stronger the induced prior is.

Moreover, cGLO provides what we call self-regularization, by reconstructing several slices at once, i.e. regularizing with the measurements themselves. Finally, cGLO does not need a backward operator like the FBP algorithm at any point to perform a CT reconstruction. The resulting approach is unsupervised and very flexible, depending on the type and quantity of available data.

As illustrated on the special case of sparse CT reconstruction, cGLO can be used as a plug-and-play reconstruction method. This article demonstrates that cGLO is a parsimonious reconstruction method that outperforms current state-of-the-art unsupervised IIPs solvers in most data regimes.

2 Methods

2.1 Computed Tomography (CT)

Given a narrow beam of X-ray photons of energy $E \in [0, \varepsilon]$, with a normalized dose spectrum $S(E)$, tracing through a material m with homogeneous density distribution ρ_m , the beam intensity decreases in accord with the Beer-Lambert law:

$$\frac{I}{I_0} = \int_0^\varepsilon S(E) \exp \left[-\left(\frac{\mu_m}{\rho_m} \right)_E \rho_m L \right] dE \quad (1)$$

where I_0 and I are respectively the input and observed intensities, L is the beam path length and μ_m the linear attenuation coefficient of material m . The ratio $\left(\frac{\mu_m}{\rho_m} \right)_E$ corresponds to the mass attenuation of material m . Depending on the energy level E , this macroscopic attenuation is obtained by adding up the effect of several absorption and scattering mechanisms, e.g. Rayleigh and Compton scattering, photoelectric absorption or pair production.

In medical tomodensitometry, the quantity of interest is the heterogeneous density distribution reflecting the patient internals. However, further assumptions are made to recover this distribution from experimental measurements: bones and other tissues are reduced to one equivalent material with water mass attenuation and the X-ray beam is considered monoenergetic.

Now, by considering an horizontal plane section through the patient body, i.e. a slice x , and by moving the source and detector as indicated in figure 1, it is possible to obtain a profile y , on the detector axis p , for the viewing angle ϕ :

$$y(p, \phi) = -\log \left(\frac{I}{I_0} \right) = \int_L x \, ds \quad (2)$$

For continuous p and ϕ the profiles y may be identified with the two-dimensional Radon transform [1, 55-65], also called the forward operator

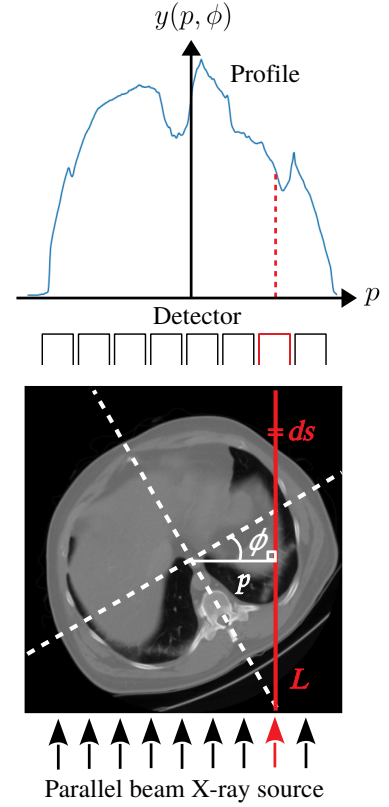


Figure 1: Parallel beam geometry profile acquisition for one viewing angle

\mathcal{T} , of the slice x , such that $y = \mathcal{T}(x)$. However, in practical use cases, projection profiles are acquired for a set of incremental values $\Phi = \phi_1, \dots, \phi_N$, which constitutes a sampling of the Radon transform. Moreover, shot noise following a Poisson process τ usually appears in experimental profiles for lower doses. Resulting experimental measurements can then be described by:

$$y_\Phi = \mathcal{T}_\Phi(x) + \tau \quad (3)$$

Given a number of viewing angles close to the Nyquist sampling criterion [40, 72-74], and sufficiently low noise, the inverse of the sampled Radon transform \mathcal{T}_Φ^\dagger can be computed with standard methods, e.g. FBP, to retrieve the slice density map without producing artefacts. By stacking several slices, the two-dimensional information may be converted to three-dimensional information.

In the case of insufficient viewing angles, e.g. sparse CT, or in presence of too much noise, e.g. low-dose CT, the inverse problem becomes ill-posed. It is classically solved using iterative optimization algorithm [41] using a *Maximum A Posteriori* (MAP) formulation of the problem:

$$x^* = \arg \min_x \|\mathcal{T}_\Phi(x) - y_\Phi\|_2^2 + \mathcal{R}(x) \quad (4)$$

where \mathcal{R} is a real valued function used to regularize the optimization process by injecting prior information on the desired output x^* . Most common operators encountered in the literature to model this information are $\|x\|_1$, $\|x\|_2$ and Total Variation (TV), $\text{TV}(x) = \|\nabla x\|_1$.

2.2 Conditioning a Score-Based Generative Model (cSGM)

The method developed by Song et al. [15] is generative. With a dataset of i.i.d. samples $\mathbf{x} \in X$ from an unknown distribution $p(\mathbf{x})$, it aims at generating new data samples. To this end, it firstly defines a continuous diffusion process, that progressively perturbs samples from $p(\mathbf{x})$ into samples from a tractable prior distribution. It is formulated as a linear SDE as follows:

$$d\mathbf{x}_t = f(t)\mathbf{x}_t dt + g(t)d\mathbf{w}_t \quad (5)$$

where $t \in [0, 1]$, dt is an infinitesimal time step, f and g are real valued functions, \mathbf{w}_t is a standard Wiener process, and \mathbf{x}_t represents the samples through the perturbation process. The marginal probability distribution of \mathbf{x}_t , $p_t(\mathbf{x}_t)$ can be further derived from Eq. (5), as well as the transition distribution from \mathbf{x}_0 to \mathbf{x}_t , $p_{0t}(\mathbf{x}_t|\mathbf{x}_0)$. f and g are carefully designed so that, for any $p_0(\mathbf{x}) \equiv p(\mathbf{x})$, Eq. (5) ensures convergence at $t = 1$ towards a distribution $p_1(\mathbf{x})$ close to a Gaussian noise.

As demonstrated by Anderson [42], the reverse of the diffusion process, in Eq. (5), is also a diffusion process which can be written as the following reverse-time SDE:

$$d\mathbf{x}_t = [f(t)\mathbf{x}_t + g(t)^2 \nabla_{\mathbf{x}_t} \log p_t(\mathbf{x}_t)] dt + g(t)d\bar{\mathbf{w}}_t \quad (6)$$

where $\bar{\mathbf{w}}_t$ is a standard Wiener process in the reverse-time direction, and dt indicates an infinitesimal negative time step. Solving Eq. (6) from $t = 1$ to $t = 0$ corresponds to a continuous denoising, yielding data samples $\mathbf{x}_0 \sim p_0(\mathbf{x}) \equiv p(\mathbf{x})$ from noise samples [15]. However, it requires the score function $\nabla_{\mathbf{x}_t} \log p_t(\mathbf{x}_t)$ of $p_t(\mathbf{x}_t)$. Using a time-dependent neural network $s_\theta(\mathbf{x}, t)$ called the score model, it is learned on X with denoising score matching. As described in [43] and [15], the score model is trained by approximating the known score functions of the transition distributions from \mathbf{x}_0 to \mathbf{x}_t , $p_{0t}(\mathbf{x}_t|\mathbf{x}_0)$. Optimized parameters θ^* ensure that $s_{\theta^*}(\mathbf{x}, t) \approx \nabla_{\mathbf{x}_t} \log p_t(\mathbf{x}_t)$ according to denoising score matching theory. The score model can then be plugged into Eq. (6), yielding:

$$d\mathbf{x}_t = [f(t)\mathbf{x}_t + g(t)^2 s_{\theta^*}(\mathbf{x}, t)] dt + g(t)d\bar{\mathbf{w}}_t \quad (7)$$

from here, one can sample from $p_0(\mathbf{x})$ using a sequence of time steps $0 = t_0 < t_1 < \dots < t_N = 1$ with standard iterative sampling techniques:

$$\mathbf{x}_{t_{i-1}} = \mathbf{h}(\mathbf{x}_{t_i}, \mathbf{z}_i, s_{\theta^*}(\mathbf{x}_{t_i}, t_i)) \quad (8)$$

where $\mathbf{z}_i \sim \mathcal{N}(\mathbf{0}, \mathbf{I})$ and \mathbf{h} denotes the iterative function related to the chosen sampling algorithm, such as annealed Langevin dynamics [10] or Predictor-Corrector samplers [15].

Although it is natural to *unconditionally* sample from Eq. (7), conditioning the sampling process to measurements, i.e. being able to sample from the posterior distribution $p(\mathbf{x}|\mathbf{y})$, is not trivial. Building on the unconditional case, Song et al. [16] introduce perturbed measurements \mathbf{y}_t given the experimental observation \mathbf{y} . They design an iterative sampling algorithm that promotes, at each time-step t_i , consistency of *conditioned* samples \mathbf{x}'_{t_i} simultaneously with the perturbed measurements \mathbf{y}_{t_i} and the *unconditioned* samples \mathbf{x}_{t_i} by solving a proximal optimization step:

$$\mathbf{x}'_{t_i} = \arg \min_w \{(1 - \lambda) \|w - \mathbf{x}_{t_i}\|_{\mathcal{T}_{\phi_e}}^2 + \lambda \min_u \|w - u\|_{\mathcal{T}_{\phi_e}}^2\} \quad s.t. \quad \mathcal{T}_{\phi_e}(u) = \mathbf{y}_{t_i} \quad (9)$$

where \mathcal{T}_{ϕ_e} is the Radon transform sampled on ϕ_e , the set of experimental viewing angles, and $\|\cdot\|_{\mathcal{T}}^2 = \|\mathcal{T}(\cdot)\|_2^2$. The hyper-parameter $\lambda \in [0, 1]$ balances consistency regarding experimental measurements ($\lambda \rightarrow 1$) and *unconditioned* samples ($\lambda \rightarrow 0$).

Song et al. [16] demonstrated that Eq. (9) has a tractable closed-formed solution, such that in practice, *conditioned* samples are computed through:

$$\mathbf{x}'_{t_i} = \mathcal{T}_{\Phi}^{\dagger} [P_{\phi_e}(\lambda \mathbf{y}_{t_i} + (1 - \lambda) \mathcal{T}_{\phi_e}(\mathbf{x}_{t_i})) + P_{\phi_s} \circ \mathcal{T}_{\phi_s}(\mathbf{x}_{t_i})] \quad (10)$$

where the set ϕ_e of experimental viewing angles is completed with simulated viewing angles ϕ_s to constitute an appropriate sampling, $\Phi = \phi_e \cup \phi_s$, above the Nyquist criterion, so that the inverse Radon transform $\mathcal{T}_{\Phi}^{\dagger}$ is well-defined. P denotes a profile padding operator ensuring dimensionality consistency.

Given *conditioned* samples \mathbf{x}'_{t_i} , at time-step t_i , the same iterative sampling strategy as Eq. (8) is applied to draw *unconditioned* samples $\mathbf{x}_{t_{i-1}}$:

$$\mathbf{x}_{t_{i-1}} = \mathbf{h}(\mathbf{x}'_{t_i}, \mathbf{z}_i, s_{\theta^*}(\mathbf{x}_{t_i}, t_i)) \quad (11)$$

where $s_{\theta^*}(\mathbf{x}, t)$ is the score model trained on X in an unsupervised manner, i.e. without assuming any measurement process. The reconstruction is ultimately computed by iterating sequentially on steps described in Eq. (11) and Eq. (10).

2.3 Deep Image Prior (DIP)

Ulyanov et al. [31] introduced DIP to solve classic IIPs such as denoising and super-resolution. The core idea of DIP is to regularize IIPs by taking advantage of the structural bias of a U-Net [32] f_{θ} parameterized with a set of weights θ . It operates through two mechanisms: reparameterization and early stopping (*ES*). For instance, in the case of denoising, the optimization problem is reparametrized as:

$$x^* = \{f_{\theta^*}(z) \mid \theta^* = \arg \min_{\theta} \|f_{\theta}(z) - (x_0 + \eta)\|_2^2\} \quad (12)$$

where x_0 is the initial image perturbed with unknown white noise η and z is a fixed white noise with the same dimensions as x_0 . Experiments in [31] showed that given sufficient capacity and time/iterations, via gradient descent, the randomly initialized and over-parameterized U-Net can fit the output signal almost perfectly, including the noise η . However, Ulyanov et al. [31] demonstrated that the weights descent sequence $\theta_1, \dots, \theta_N$, with $f_{\theta_N} \approx x_0 + \eta$, contains an early stopping point θ_{ES} , such that $f_{\theta_{ES}} \approx x_0$. This phenomenon has been proven to be a consequence of the structure of the generative network, more specifically the convolutional and upsampling layers [33, 34]. They induce a spectral bias in which the decoder learns to construct the image from low to high frequencies, meaning that with an appropriate choice of *ES*, one can prevent the decoder from fitting the high frequency perturbations.

This methodology has recently been tailored to reconstruct 3D CT volumes by Baguer et al. [35], using an adaptation of Eq. (12) further regularized with TV:

$$x^* = \{f_{\theta^*}(z) \mid \theta^* = \arg \min_{\theta} \|\mathcal{T}_{\phi_e} \circ f_{\theta}(z) - y_{\phi_e}\|_2^2 + \alpha \text{TV} \circ f_{\theta}(z)\} \quad (13)$$

where \mathcal{T}_{ϕ_e} is the Radon transform sampled on experimental viewing angles ϕ_e , y_{ϕ_e} are the experimental measurements and α is an hyper-parameter balancing the regularization. In this formulation, the issue of finding an appropriate early

stopping for denoising is replaced with the necessity to find an optimal value for α , depending on the ill-posedness of the IIP at hand.

Further experiments in [35] showed improvements by initializing the decoder weights using the result x_s of a supervised method, e.g. Learned Primal-Dual reconstruction [3]:

$$\theta_0 = \arg \min_{\theta} \|f_{\theta}(z) - x_s\|_2^2 \quad (14)$$

However, replacing random weights of the decoder with such an initialization restricts the applicability of the approach to the supervised use case, i.e. fixed acquisition parameters.

2.4 Generative Latent Optimization (GLO)

Attempting to generate competitive results when compared to samples from GANs without using an adversarial training protocol, Bojanowski et al. [36] proposed a novel approach consisting in mapping one freely *learned* unit latent vector z_i to each image x_i of a given dataset $X = \{x_1, \dots, x_N\}$, through a decoder network f_{θ} with parameters θ , e.g. a DCGAN [44]. With gradient descent, it comes to jointly learn decoder network parameters and latent codes $Z = \{z_1, \dots, z_N\}$, both randomly initialized, with the objective function:

$$Z^*, \theta^* = \arg \min_{Z, \theta} \frac{1}{N} \sum_{i=1}^N \|f_{\theta}(z_i) - x_i\|_2^2 \quad s.t. \quad \|z_i\|_2 = 1 \quad (15)$$

It is mentioned in [36] that, as is conventionally done for training GANs, vectors sampled from an n-dimensional normal distribution are close to the surface of an n-sphere with radius \sqrt{n} . Following this idea, during the optimization process, the latent vectors are constrained to the unit n-sphere by projection after each update.

Experiments in [36] and [37], have shown that the GLO approach does not suffer from mode collapse and significantly outperform GANs when trained on small datasets. However, like Variational Auto-Encoders (VAE) [45], the quality of generated samples deteriorates when the data variability overcomes the network capacity [46]. We also observe this behaviour in our own experiments.

2.5 Conditioning GLO (cGLO)

The method proposed to solve IIPs in this article builds on the framework described by GLO [36]. Attempting to invert GLO, i.e. sampling or exploring the manifold entailed by latent vectors learned through Eq. (15), is not straightforward [38, 39]. The latent vectors are not uniformly distributed on the surface of the n-sphere. Furthermore, the decoder generation quality rapidly worsens when evaluated on vectors outside geodesic interpolation lines between pairs of latent vectors. In other words, the manifold on which the trained decoder can produce plausible images can be described as a complete graph, heterogeneously distributed on the surface of the unit n-sphere.

Instead of inverting GLO, our method cGLO uses a reparameterization of the IIP, like DIP [31], to benefit from the structural bias of the convolutional decoder. However, the objective function described in Eq. (13), is cast into the framework of GLO [36], detailed in Eq. (15) such that the reconstruction is composed of two steps.

Firstly, given availability of previous full-dose CT scan reconstructions, i.e. a set of slices $X = \{x_1, \dots, x_N\}$, prior knowledge may be enforced by learning an appropriate initial set of parameters θ_0 , for the decoder f_{θ} , in an unsupervised manner following Eq. (14) and Eq. (15):

$$\theta_0 = \arg \min_{Z, \theta} \frac{1}{N} \sum_{i=1}^N \|f_{\theta}(z_i) - x_i\|_2^2 \quad s.t. \quad \|z_i\|_2 = 1 \quad (16)$$

Secondly, at examination time, the K slices $\bar{X} = \{\bar{x}_1, \dots, \bar{x}_K\}$ corresponding to experimental measurements are reconstructed together such that the parameters θ , and the latent unit vectors $\bar{Z} = \{\bar{z}_1, \dots, \bar{z}_K\}$ are jointly learned through:

$$\bar{Z}^*, \theta^* = \arg \min_{\bar{Z}, \theta} \frac{1}{K} \sum_{i=1}^K \|\mathcal{T}_{\phi_e} \circ f_{\theta}(\bar{z}_i) - y_{i, \phi_e}\|_1^2 \quad s.t. \quad \|\bar{z}_i\|_2 = 1 \quad (17)$$

$$\bar{X}^* = f_{\theta^*}(\bar{Z}^*) \quad (18)$$

where \mathcal{T}_{ϕ_e} is the Radon transform sampled on experimental viewing angles ϕ_e and y_{i, ϕ_e} are the profiles obtained from slice \bar{x}_i . Because of the shared decoder between the entire set of slice reconstructions \bar{X}^* , and with sufficient slices to reconstruct, this strategy avoids the overfitting issue of DIP. It is expected for the set of parameters θ_0 to be closer to θ^* than random weights, thus easing the optimization of Eq. (17), especially when ϕ_e is very sparse. The latent vectors from Eq. (16) are not reused so that the set \bar{Z} of Eq. (17) is always randomly initialized.

Consequently, cGLO is an unsupervised reconstruction methodology that is very flexible as it can be adapted to various practical use cases regardless of the quantity of data at hand.

3 Experiments

3.1 Datasets

Experiments are conducted on two commonly used datasets which are publicly available on The Cancer Imaging Archive (TCIA) platform [47]. The Lung Image Database Consortium (LIDC) [48] image collection was collected using lung cancer screenings from 1018 patients. It consists of thoracic CT scans completed with radiologists annotations for nodule segmentation. The Low-dose CT image and projection dataset (LDCT) [49] is comprised of 299 CT scans of patients heads, chests and abdomens and their respective (full) clinical doses. In addition, the LDCT dataset also includes simulated reduced doses, by Poisson noise insertion, and the location and diagnosis for positive findings. In the presented experiments, only CT scan slices from both datasets are used. Depending on the optimization process, slices are either directly compared using a pixel-wise metric, or indirectly via simulated measurements obtained from the application of the same forward operator, i.e. a full dose parallel-beam geometry with viewing angles equally distributed across 180 degrees. Similarly to Song et al. [16], our approach treats every slice independently. Therefore, though 3D scan geometric parameters such as pixel spacing and slice thickness may vary across patients, slices are not resampled, such that 3D volumes can have different number of slices and spatial scales. The native resolution of slices is 512x512 pixels for both datasets, but the LIDC slices are downsized to a resolution of 320x320 pixels. For experiments to be representative of various realistic situations with sparse or abundant data, training sub-datasets consisting of portions of the LIDC and LDCT collections are prepared. Details of such datasets are given in table 1. The LIDC and the LDCT test sets consist of 5 scans respectively totalling 791 and 1089 slices. Unless stated otherwise, Peak Signal to Noise Ratio (PSNR) and Structural SIMilarity (SSIM) metrics are estimated on the total test set where each 3D volume is reconstructed independently, meaning that 5 independent reconstructions are computed.

Portion	# of scans	# of slices
50%	500	104 953
35%	350	65 033
20%	200	35 697
10%	100	17 898
2%	20	2 906

(a) LIDC sub-datasets

Portion	# of scans	# of slices
50%	147	24 464
35%	103	16 924
20%	59	10 463
10%	29	4 989
2%	6	930

(b) LDCT sub-datasets

Table 1: Sub-datasets used for training with their corresponding number of 3D scans and slices. 3D scans are always fully included.

3.2 Implementation Details

In the presented experiments, the geometry of the decoder's latent space is set to the unit n-sphere, similarly to state-of-the art representation learning approaches [36]. The latent space dimension is set to 320 for experiments on the LIDC dataset and 512 for the LDCT dataset. Being a reference in the literature of generative models, the Deep Convolutional Generative Adversarial Network (DCGAN) [44] architecture is used for the decoder. As illustrated in figure 2, the latent code firstly goes through a linear block and is mapped to a feature map of shape $2 \times 2 \times C$, with C the desired number of channels for the first convolutional layer. From layer to layer the input is upsampled by a factor 2 (last layer upscale factor may vary to fit the desired output image resolution) and the number of channels is cut by half. Hence, the image resolution, the latent dimension and C completely define the structure of the decoder. The number of input channels C is set to 8192 for both experiments on the LIDC and the LDCT sub-datasets.

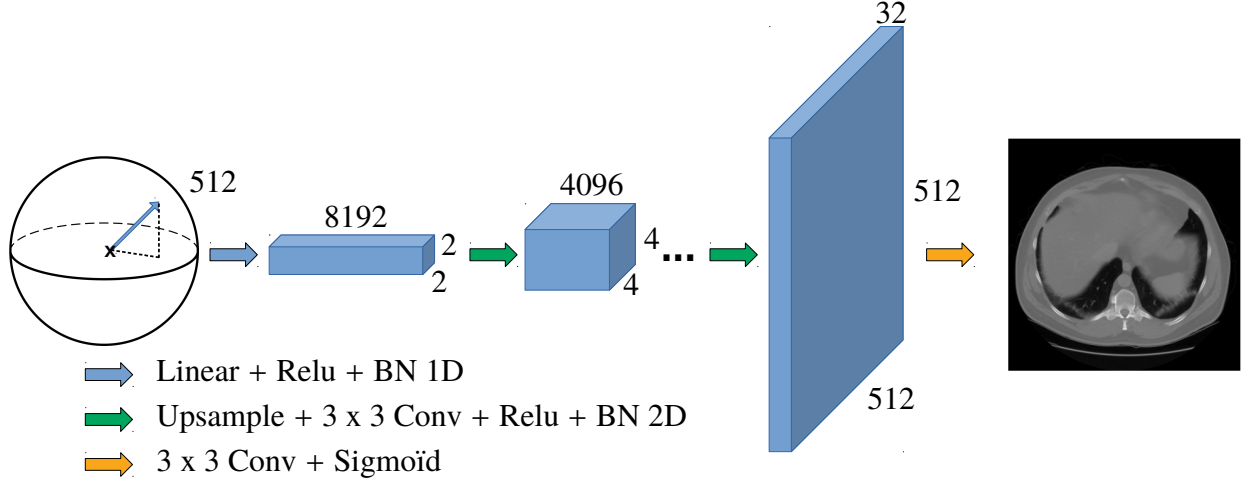


Figure 2: Generator DCGAN-like architecture, latent dimension (512) and final resolution (512x512) correspond to the LDCT sub-datasets experiments.

Optimizations are conducted with the Adam algorithm [50], with parameters kept at default values. The learning rates for the latent codes and the decoder weights are both set to 10^{-3} while training on CT reconstruction, i.e. the first step described in Eq. (16), and respectively set to 10^{-2} and 10^{-4} when reconstructing from experimental measurements, i.e. the second step as shown in Eq. (17). Although learning rates are kept constant, batch sizes are increased along specified schedules. It leads to faster training and is statistically equivalent to decreasing learning rates [51]. Finally, the optimization described in Eq. (17) is further stabilized by artificially augmenting the number of experimental measurements, with a linear interpolation along the vertical axis, i.e. the axis orthogonal to the slices plane. It simulates a larger set of experimental measurements, which includes true experimental measurements. Reconstructions are conducted using the entire augmented set, then reconstructions corresponding to interpolated measurements are discarded. Practically, measurements are augmented by a factor 8 for reconstructions conducted on both the LIDC and the LDCT test sets.

Regarding cSGM, hyper-parameters, model architecture and other implementation details are set to what is provided by Song et al. [16] for sparse-view CT experiments.

3.3 Results

In this section, our method cGLO is compared to cSGM [16], which currently achieves state-of-the-art performance for unsupervised sparse CT. The two approaches are compared on quantitative pixel-wise (PSNR) and structural (SSIM) metrics which are given in figure 3 and detailed in Table 2 for reconstructions computed from 100 experimental viewing angles. Qualitative results consists of examples of reconstructions from cGLO and cSGM trained on the smallest sub-dataset consisting of a 2% portion of the LIDC and the LDCT datasets. These reconstructions from the LIDC and the LDCT test sets are respectively presented in figure 4 and figure 5. Additional results and examples, for experimental setups corresponding to different combinations of training dataset sizes and number of viewing angles are provided in appendix A and B.

3.3.1 Quantitative performance

As shown in figure 3, cGLO outperforms cSGM in most data and viewing angles regimes. cSGM achieves better median PSNR values only in scenarios involving more than 100 experimental viewing angles, when the portion of the employed sub-datasets is superior to 20%. The details of the performance of both models in this context are presented in table 2. In every other experimental setups, our method cGLO outperforms cSGM regarding median PSNR values. Furthermore, cGLO achieves higher median SSIM metrics values in all experimental setups, even in abundant data regimes with large training sub-datasets and many experimental viewing angles. Also, median PSNR and especially median SSIM curves in figure 3 indicate that the performance gap, at the advantage of cGLO over cSGM, increases as the set of experimental viewing angles gets sparser and/or the training dataset gets smaller. In other words, our method is more parsimonious and more robust for solving increasingly sparse CT when compared to cSGM.

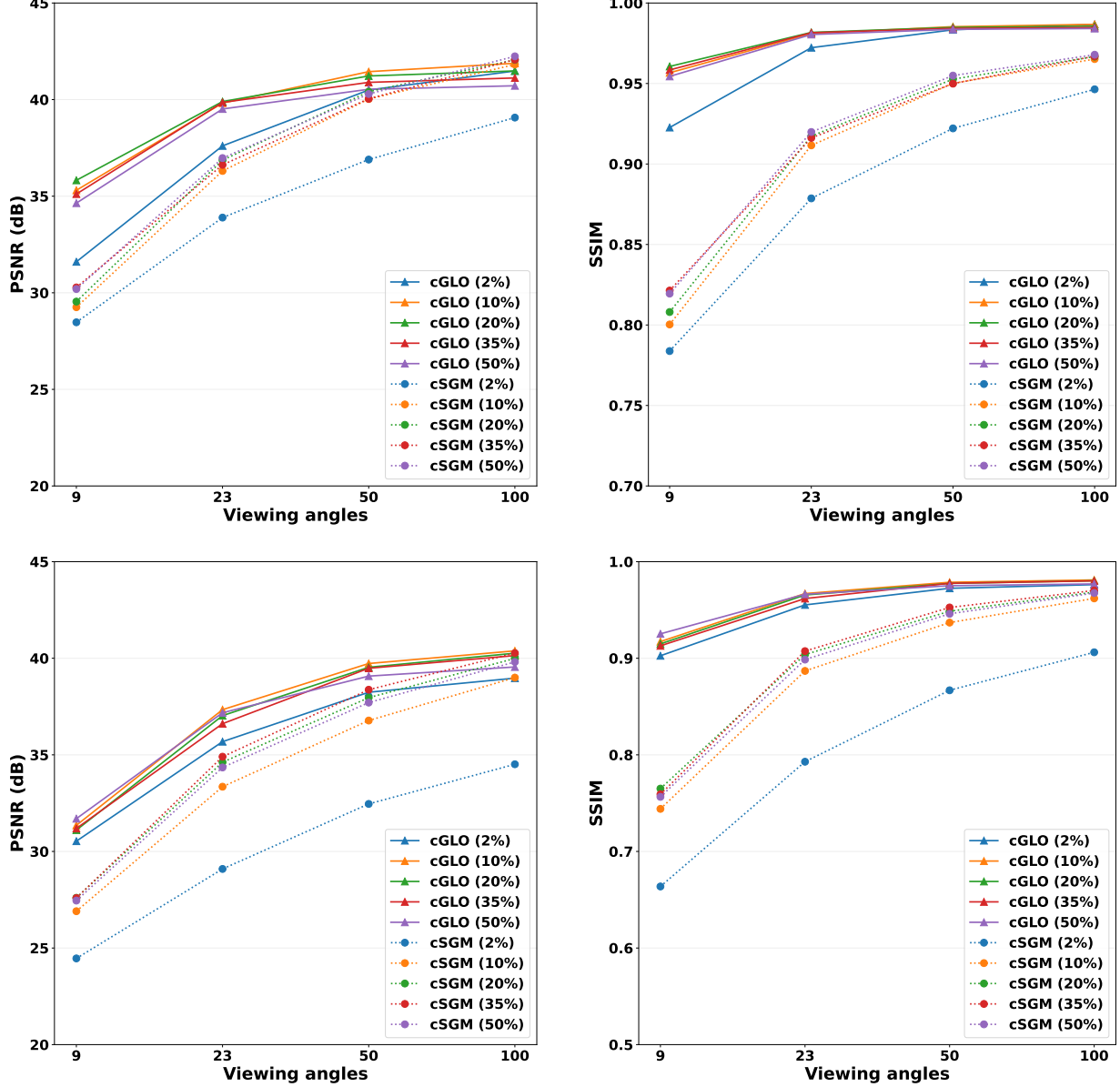


Figure 3: PSNR (left side) and SSIM (right side) median values curves corresponding to reconstructions of slices from the LIDC dataset (upper row) and the LDCT dataset (lower row) test sets given 9, 23, 50 and 100 experimental viewing angles. Each curve is associated with one of the training sub-datasets presented in table 1.

3.3.2 Effect of training data

As illustrated in figure 3, contrary to cSGM, our model performance plateaus as the number of experimental viewing angles increases and even slightly worsens, regarding median PSNR values, as the training datasets becomes larger. Given a fixed representation capacity for our decoder architecture, i.e. a fixed number of input channels C , the model becomes under-parameterized after a given training dataset size is reached. Since the model parameters and the latent codes are jointly optimized in Eq. (16) with respect to a data-likelihood objective function, the model error distribution is widely spread over the entire training dataset [46]. Consequently, when the data variability overcomes the model capacity, each additional training example further deteriorates the average prediction quality. Ideally, the model capacity should be tuned to best fit each experimental setup. The experiments realized in this paper however demonstrate that even with a fixed decoder architecture, cGLO produces superior reconstructions for a wide range of experimental setups.

Method	Data	LIDC 320x320		LDCT 512x512	
		PSNR \uparrow	SSIM \uparrow	PSNR \uparrow	SSIM \uparrow
cSGM	2%	39.07 \pm 0.89	0.946 \pm 0.015	34.51 \pm 0.53	0.906 \pm 0.012
cGLO	2%	41.48 \pm 1.69	0.987 \pm 0.006	38.97 \pm 1.12	0.976 \pm 0.007
cSGM	10%	41.82 \pm 1.47	0.965 \pm 0.015	39.00 \pm 1.08	0.962 \pm 0.008
cGLO	10%	41.88 \pm 1.64	0.987 \pm 0.006	40.38 \pm 1.45	0.981 \pm 0.006
cSGM	20%	42.06 \pm 1.61	0.967 \pm 0.014	39.99 \pm 1.18	0.969 \pm 0.008
cGLO	20%	41.48 \pm 1.55	0.986 \pm 0.006	40.26 \pm 1.61	0.980 \pm 0.007
cSGM	35%	42.07 \pm 1.67	0.967 \pm 0.013	40.27 \pm 1.18	0.970 \pm 0.007
cGLO	35%	41.12 \pm 1.44	0.985 \pm 0.006	40.14 \pm 1.47	0.980 \pm 0.007
cSGM	50%	42.24 \pm 1.64	0.968 \pm 0.013	39.81 \pm 1.08	0.968 \pm 0.008
cGLO	50%	40.72 \pm 1.39	0.984 \pm 0.006	39.55 \pm 1.15	0.977 \pm 0.006

Table 2: PSNR and SSIM median \pm half Inter Quartile Range (IQR) values for reconstructions of slices from the LIDC and the LDCT test datasets given 100 experimental viewing angles.

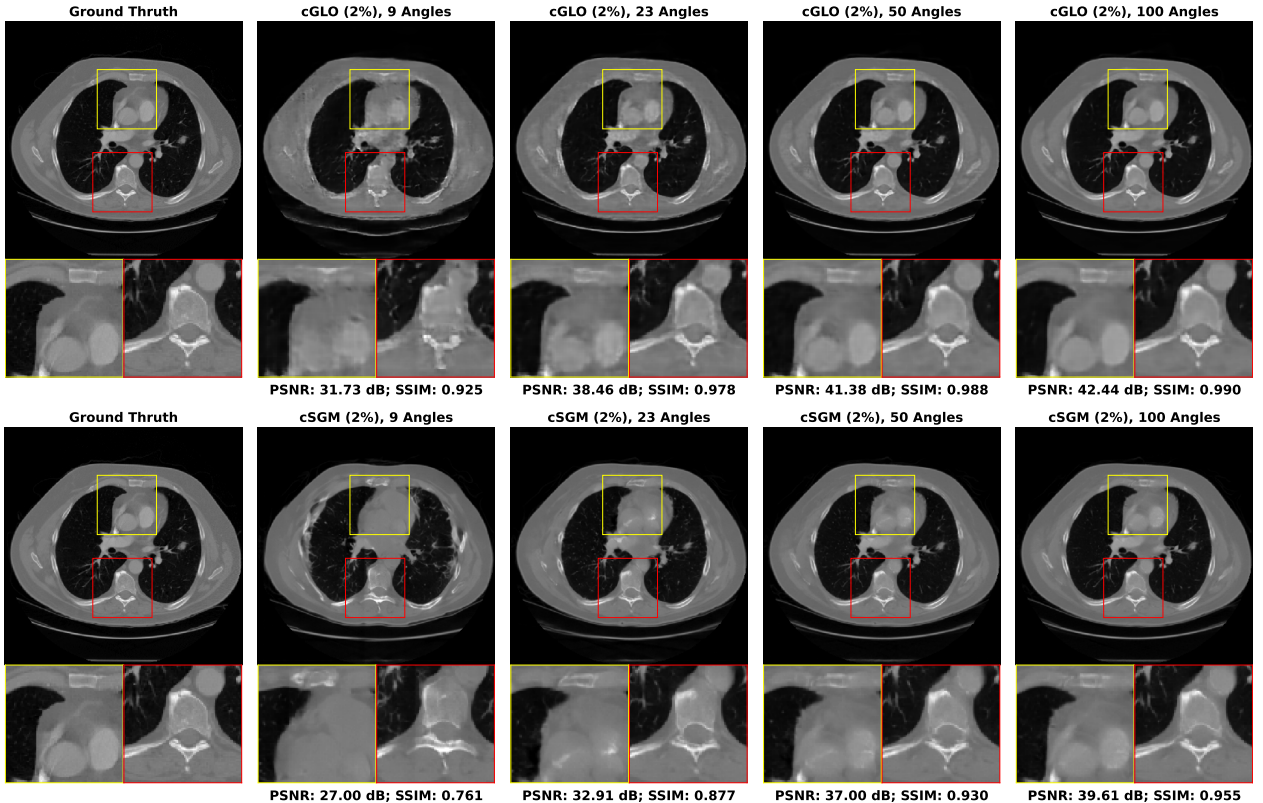


Figure 4: Examples of reconstructions given 9, 23, 50 and 100 experimental viewing angles, obtained with cGLO (upper row) and cSGM (lower row). Both methods are trained on the sub-dataset consisting of a 2% portion of the LIDC dataset.

3.3.3 Reconstruction quality

Figure 4 and figure 5 compare reconstructions computed with cGLO and cSGM respectively from the LIDC and the LDCT test datasets. Reconstruction quality clearly degrades for both models as the number of experimental viewing angles diminishes. The type of degradation, however, differs between cGLO and cSGM. While cGLO reconstructions lack sharp details and get noisier for very sparse CT, cSGM tends to alter the structural integrity of the slices. In addition, cSGM reproduces as a texture on top of its reconstructions the high frequency artefacts resulting from the FBP operator, when those exists in the training dataset, e.g. in the LDCT dataset. This effect is especially noticeable in reconstructions shown in figure 9 which may be zoomed in for more details. Our model does not show this behaviour in

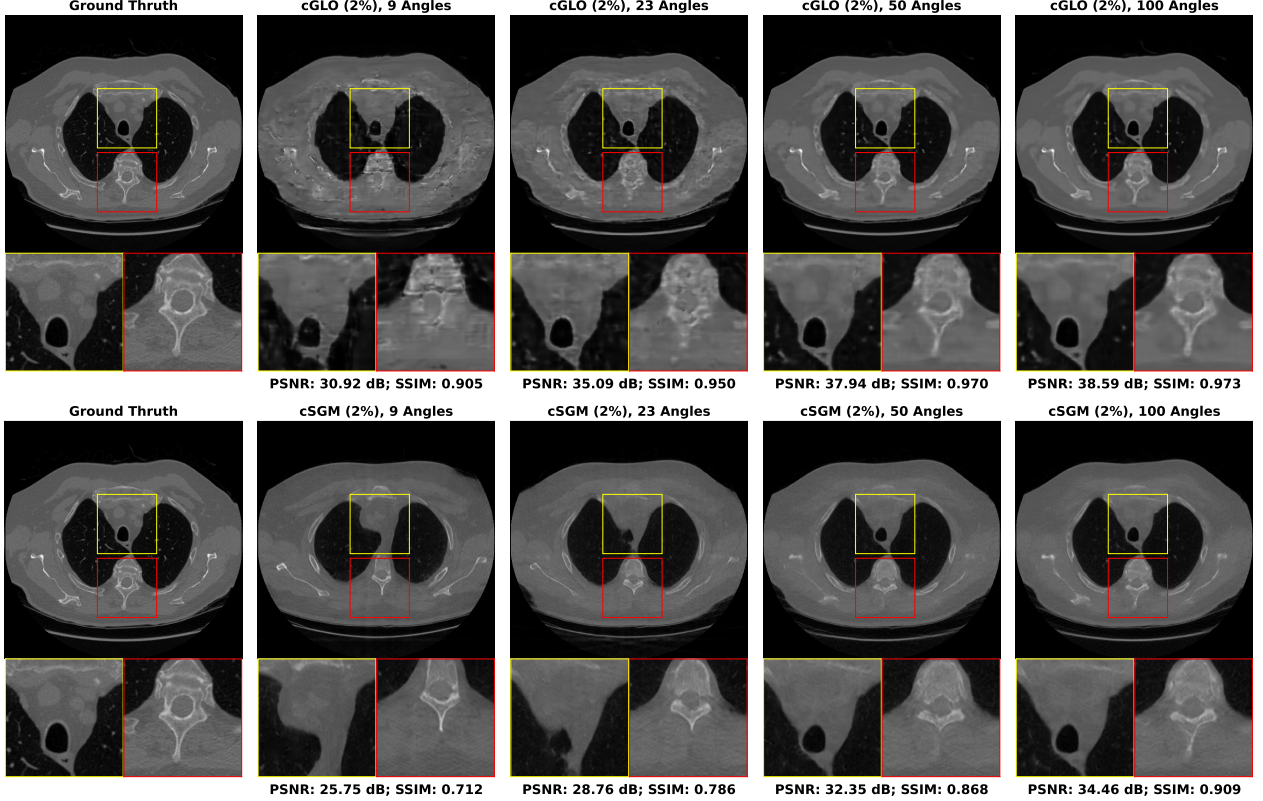


Figure 5: Examples of reconstructions given 9, 23, 50 and 100 experimental viewing angles, obtained with cGLO (upper row) and cSGM (lower row). Both methods are trained on the sub-dataset consisting of a 2% portion of the LDCT dataset.

any experiment. These two observations corroborate and explain the larger gap in performance between cGLO and cSGM when comparing median SSIM curves rather than median PSNR curves in figure 3.

The fact that cSGM and cGLO yield different reconstruction results at decreasing viewing angles can be explained by the way each model employs experimental data. cSGM uses a proximal optimization step, described in Eq. (9) to mix experimental data with unconditioned samples. The cost function of Eq. (9), expresses a balance between data likelihood and prior, which only enforces a loose constraint on the conformity of the proposed reconstruction to experimental data. When the number of viewing angles diminishes, this is responsible for the structural deformations appearing in figure 4 and figure 5.

On the contrary, the cost function of cGLO, described in Eq. (17), enforces a strict constraint on experimental data. With decreasing viewing angles, the energy landscape of this cost function becomes less smooth, leading to the presence of local minima and harder convergence of the optimization process. As seen in figure 8, this leads to degraded reconstructions with more noise and less details at 9 viewing angles for example. However, contrary to cSGM, cGLO does not tend to create hallucinated structures arising from a too strong prior.

4 Conclusion

In this work, a novel unsupervised method to solve IIPs named cGLO was presented, built upon the general framework of GLO [36]. Contrary to supervised strategies, our method does not require a fixed experimental setup. cGLO was tested on sparse-view CT which is a widely studied reconstruction problem arising in medical imaging and compared to the current state-of-the-art unsupervised reconstruction approach cSGM [16]. Experiments conducted in this paper cover a wide range of realistic setups with varying amount of available training data and experimental viewing angles. Quantitative results demonstrate that cGLO is a parsimonious and robust reconstruction method, as the performance advantage over cSGM increases for smaller training datasets and sparser experimental viewing angles. Moreover, reconstruction examples illustrate that cGLO also exhibits potentially attractive properties like a propensity to preserve

the structural integrity of reconstructions, even for very ill-posed IIPs, thanks to its straightforward conditioning to experimental measurements.

While the performance of cGLO have been tested on a tomographic reconstruction problem, the framework developed in this article can be readily applied to other ill-posed IIPs, such as MRI reconstruction from a sparsely sampled k-space, as done with cSGM. Furthermore, since the cGLO approach only requires the knowledge of the forward operator, it could in principle be extended to solve non-linear IIPs. One of the main interests of cGLO is that it does not require any backward operator, such as FBP for tomographic reconstruction. It is thus a method of choice for IIPs where such operators do not exist, such as multi-material CT reconstruction, used for example in security screening. Future work will explore the application of cGLO to such IIPs. Since cGLO efficiently learns correlations between the output channels of its decoder network, further developments will also focus on multi-task applications, such as jointly learning reconstruction and segmentation.

5 Appendix A: Quantitative results tables

Method	Data	LIDC 320x320		LDCT 512x512	
		PSNR \uparrow	SSIM \uparrow	PSNR \uparrow	SSIM \uparrow
cSGM	2%	28.47 \pm 1.04	0.784 \pm 0.027	24.46 \pm 1.10	0.664 \pm 0.059
cGLO	2%	31.60 \pm 1.30	0.923 \pm 0.016	30.53 \pm 0.98	0.903 \pm 0.014
cSGM	10%	29.25 \pm 1.00	0.800 \pm 0.020	26.91 \pm 1.08	0.744 \pm 0.041
cGLO	10%	35.31 \pm 0.94	0.957 \pm 0.008	31.35 \pm 0.99	0.917 \pm 0.017
cSGM	20%	29.54 \pm 0.88	0.808 \pm 0.022	27.60 \pm 1.15	0.765 \pm 0.036
cGLO	20%	35.82 \pm 1.50	0.961 \pm 0.009	31.11 \pm 1.03	0.915 \pm 0.015
cSGM	35%	30.28 \pm 1.13	0.821 \pm 0.031	27.59 \pm 1.31	0.759 \pm 0.038
cGLO	35%	35.11 \pm 0.97	0.958 \pm 0.006	31.19 \pm 1.08	0.913 \pm 0.016
cSGM	50%	30.19 \pm 1.16	0.819 \pm 0.033	27.46 \pm 1.05	0.757 \pm 0.035
cGLO	50%	34.64 \pm 1.41	0.954 \pm 0.009	31.70 \pm 1.18	0.925 \pm 0.014

Table 3: PSNR and SSIM median \pm half Inter Quartile Range (IQR) values for reconstructions of slices from the LIDC and the LDCT test datasets given 9 experimental viewing angles.

Method	Data	LIDC 320x320		LDCT 512x512	
		PSNR \uparrow	SSIM \uparrow	PSNR \uparrow	SSIM \uparrow
cSGM	2%	33.89 \pm 1.01	0.879 \pm 0.019	29.09 \pm 0.61	0.793 \pm 0.018
cGLO	2%	37.60 \pm 1.67	0.972 \pm 0.009	35.68 \pm 1.03	0.955 \pm 0.010
cSGM	10%	36.31 \pm 0.79	0.912 \pm 0.015	33.35 \pm 1.02	0.887 \pm 0.017
cGLO	10%	39.82 \pm 1.26	0.981 \pm 0.006	37.34 \pm 1.40	0.967 \pm 0.010
cSGM	20%	36.87 \pm 0.82	0.917 \pm 0.015	34.62 \pm 0.96	0.904 \pm 0.015
cGLO	20%	39.90 \pm 1.26	0.982 \pm 0.005	37.03 \pm 1.33	0.965 \pm 0.010
cSGM	35%	36.62 \pm 1.61	0.916 \pm 0.024	34.90 \pm 1.08	0.907 \pm 0.015
cGLO	35%	39.85 \pm 1.19	0.982 \pm 0.005	36.61 \pm 1.45	0.962 \pm 0.010
cSGM	50%	36.97 \pm 1.33	0.920 \pm 0.023	34.35 \pm 0.95	0.899 \pm 0.015
cGLO	50%	39.52 \pm 1.17	0.980 \pm 0.005	37.18 \pm 1.18	0.966 \pm 0.008

Table 4: PSNR and SSIM median \pm half Inter Quartile Range (IQR) values for reconstructions of slices from the LIDC and the LDCT test datasets given 23 experimental viewing angles.

Method	Data	LIDC 320x320		LDCT 512x512	
		PSNR \uparrow	SSIM \uparrow	PSNR \uparrow	SSIM \uparrow
cSGM	2%	36.90 \pm 0.83	0.922 \pm 0.016	32.46 \pm 0.56	0.867 \pm 0.015
cGLO	2%	40.50 \pm 1.56	0.983 \pm 0.007	38.24 \pm 1.05	0.972 \pm 0.007
cSGM	10%	40.03 \pm 1.05	0.950 \pm 0.016	36.78 \pm 0.96	0.937 \pm 0.013
cGLO	10%	41.45 \pm 1.53	0.985 \pm 0.006	39.73 \pm 1.31	0.979 \pm 0.007
cSGM	20%	40.41 \pm 1.19	0.953 \pm 0.016	37.96 \pm 1.03	0.949 \pm 0.011
cGLO	20%	41.22 \pm 1.47	0.985 \pm 0.006	39.53 \pm 1.38	0.978 \pm 0.008
cSGM	35%	40.04 \pm 1.45	0.950 \pm 0.019	38.37 \pm 1.05	0.953 \pm 0.010
cGLO	35%	40.89 \pm 1.38	0.984 \pm 0.006	39.48 \pm 1.43	0.978 \pm 0.008
cSGM	50%	40.29 \pm 1.50	0.955 \pm 0.020	37.71 \pm 1.03	0.946 \pm 0.011
cGLO	50%	40.53 \pm 1.35	0.984 \pm 0.006	39.08 \pm 1.12	0.975 \pm 0.006

Table 5: PSNR and SSIM median \pm half Inter Quartile Range (IQR) values for reconstructions of slices from the LIDC and the LDCT test datasets given 50 experimental viewing angles.

6 Appendix B: Reconstruction examples

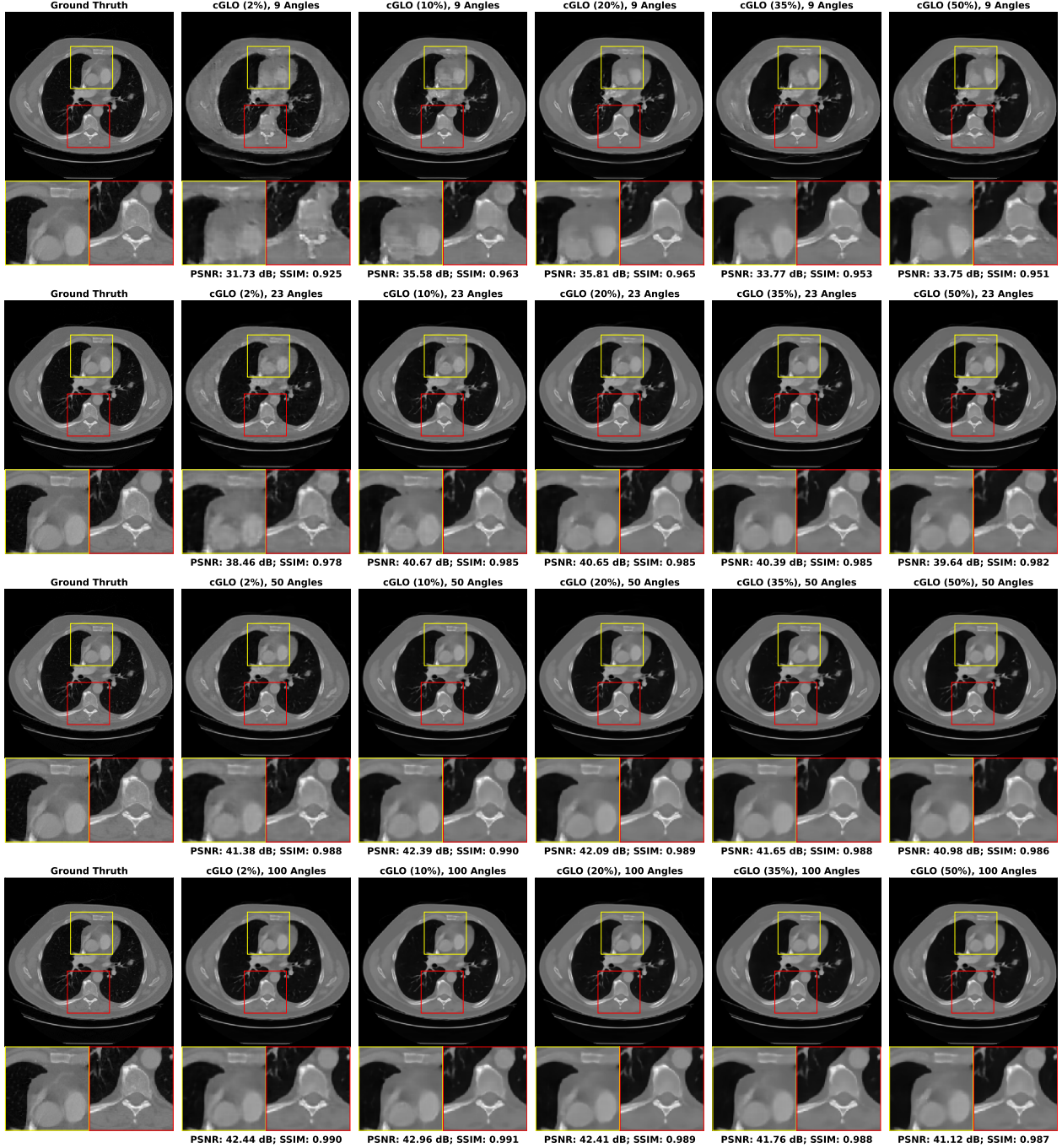


Figure 6: Examples of reconstructions of slices from the LIDC test set given : 9, 23, 50 and 100 experimental viewing angles. They are obtained with cGLO trained on the following portions of the LIDC dataset : 2%, 10%, 20%, 35% and 50%.

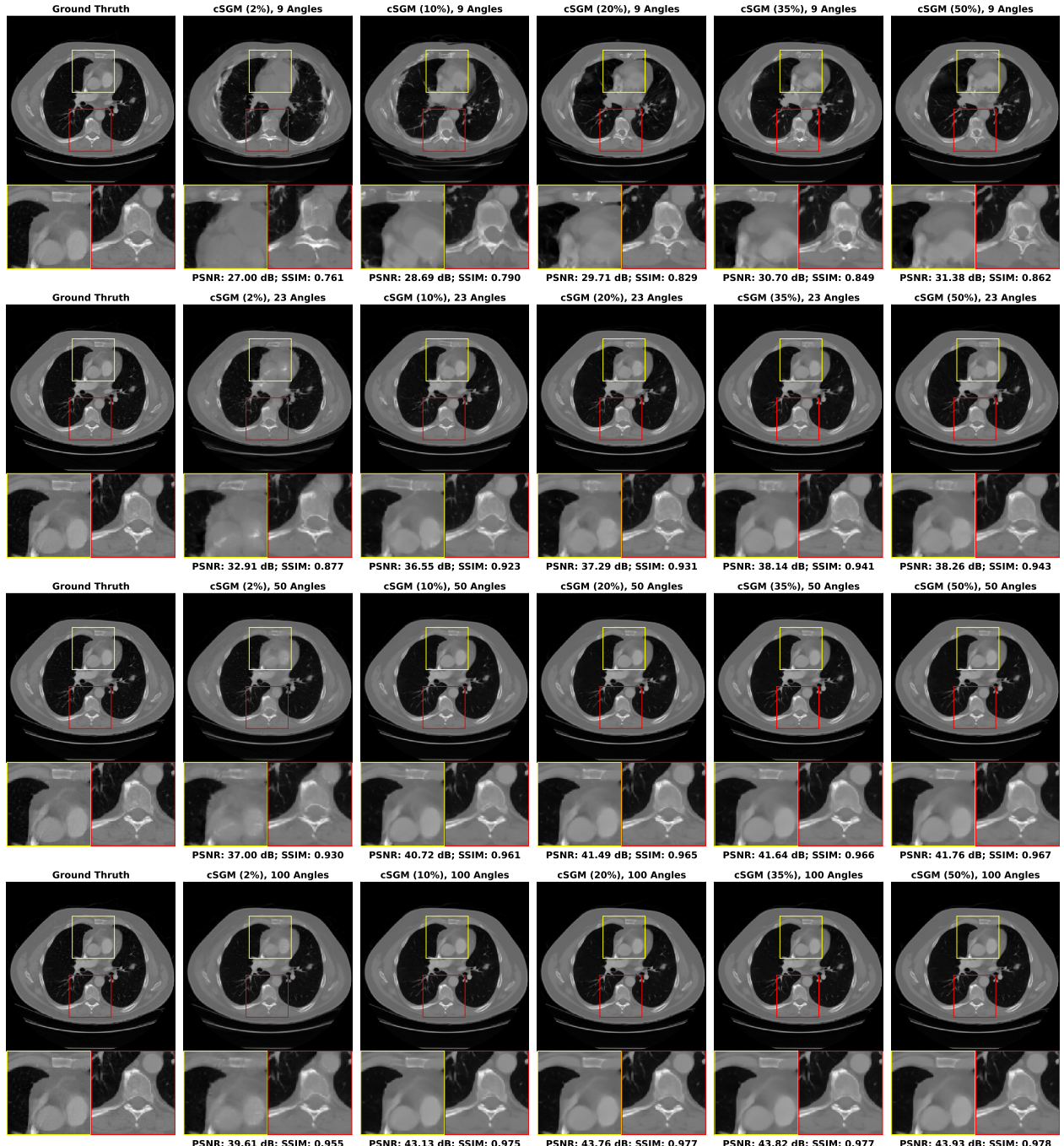


Figure 7: Examples of reconstructions of slices from the LIDC test set given : 9, 23, 50 and 100 experimental viewing angles. They are obtained with cSGM trained on the following portions of the LIDC dataset : 2%, 10%, 20%, 35% and 50%.

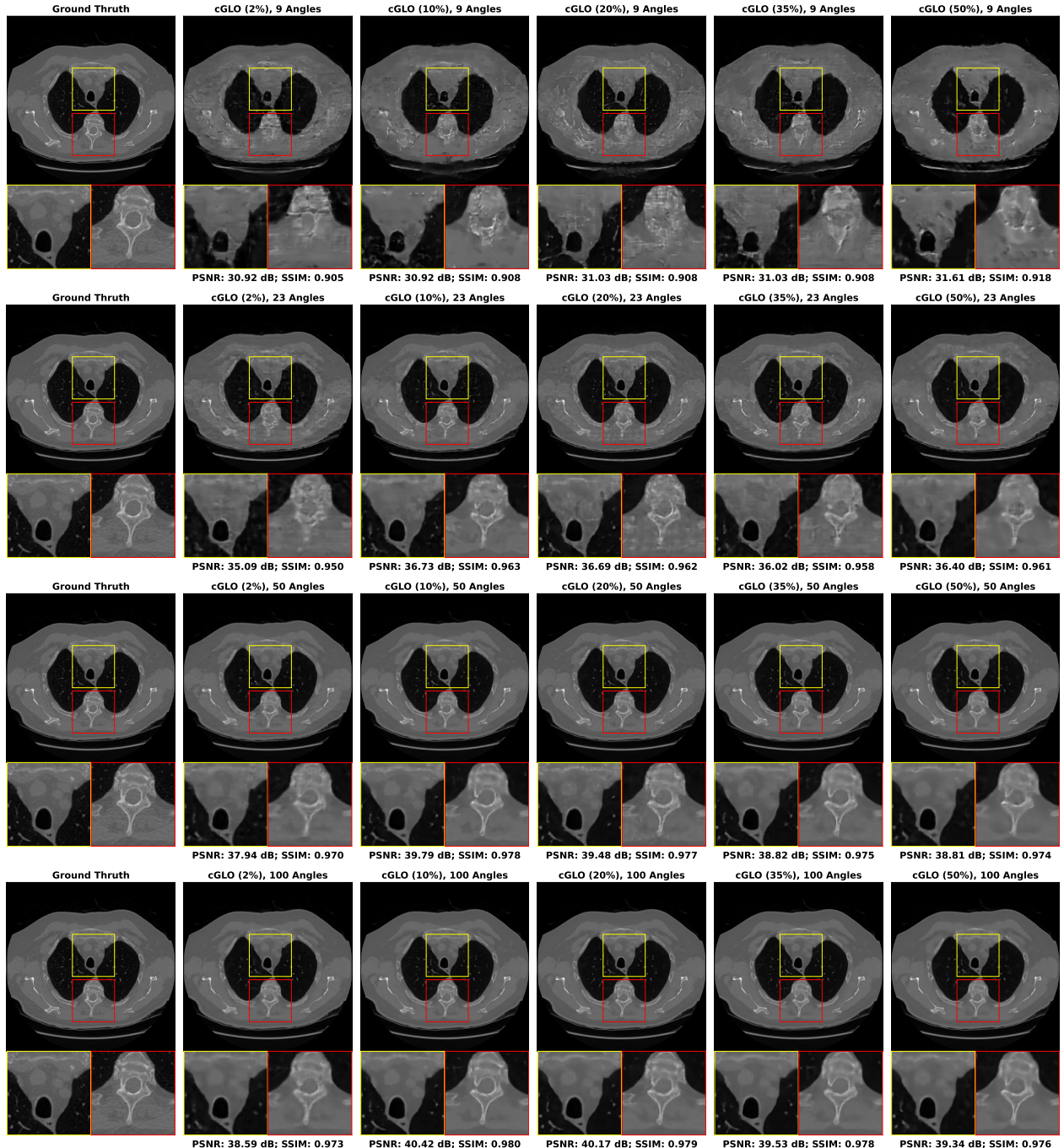


Figure 8: Examples of reconstructions of slices from the LDCT test set given : 9, 23, 50 and 100 experimental viewing angles. They are obtained with cGLO trained on the following portions of the LDCT dataset : 2%, 10%, 20%, 35% and 50%.

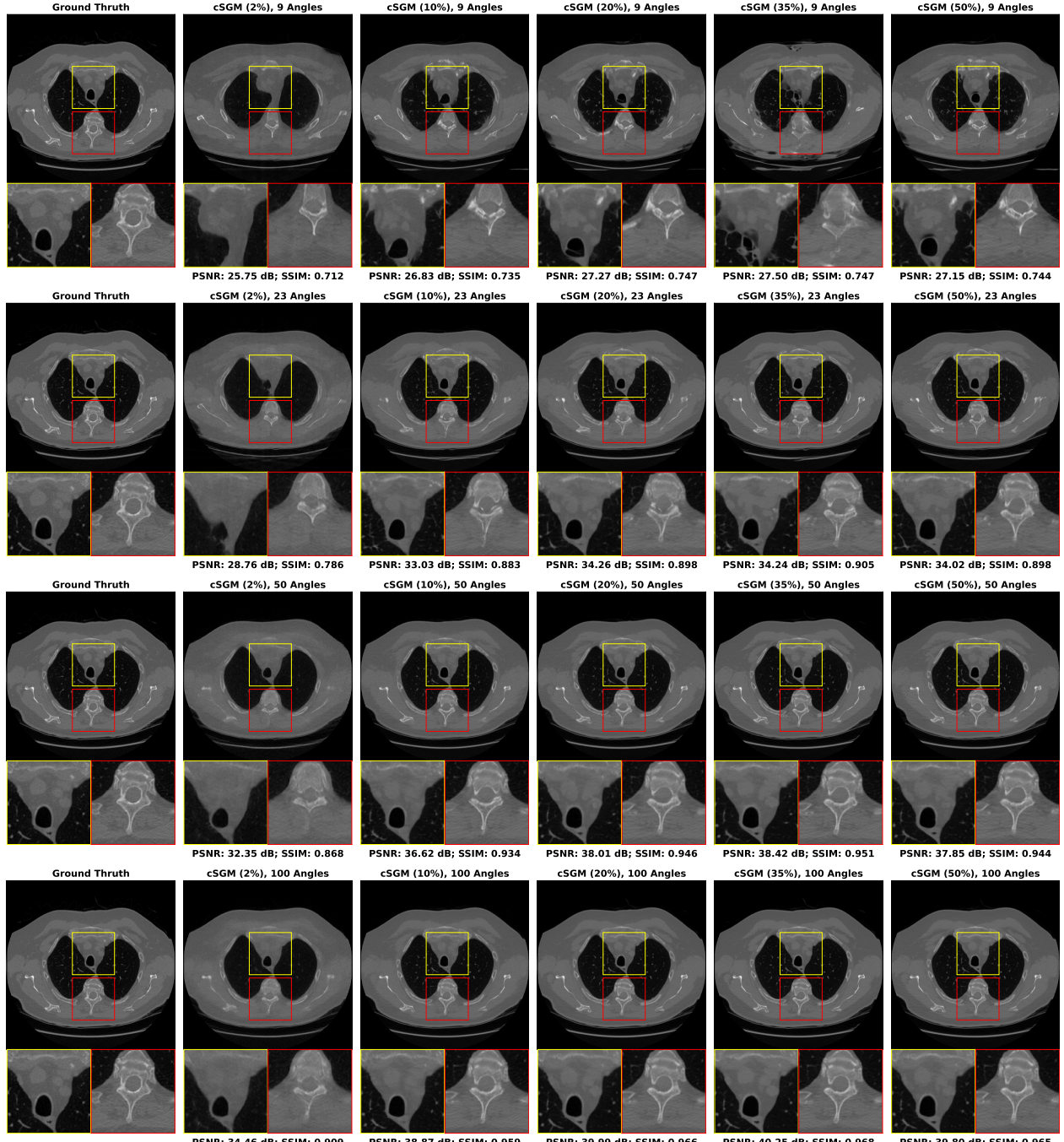


Figure 9: Examples of reconstructions of slices from the LDCT test set given : 9, 23, 50 and 100 experimental viewing angles. They are obtained with cSGM trained on the following portions of the LDCT dataset : 2%, 10%, 20%, 35% and 50%.

References

- [1] Stanley R. Deans. *The Radon transform and some of its applications*. Wiley, 1983.
- [2] Jonas Adler and Ozan Öktem. Deep Bayesian Inversion. 2018. arXiv:1811.05910 [stat.ML].
- [3] Jonas Adler and Ozan Öktem. Learned Primal-Dual Reconstruction. *IEEE Transactions on Medical Imaging*, 37(6):1322–1332, 2018. doi: 10.1109/TMI.2018.2799231.
- [4] Hoyeon Lee, Jongha Lee, Hyeongseok Kim, Byungchul Cho, and Seungryong Cho. Deep-Neural-Network-Based Sinogram Synthesis for Sparse-View CT Image Reconstruction. *IEEE Transactions on Radiation and Plasma Medical Sciences*, 3(2):109–119, 2019. doi: 10.1109/TRPMS.2018.2867611.
- [5] Bo Zhu, Jeremiah Z. Liu, Stephen F. Cauley, Bruce R. Rosen, and Matthew S. Rosen. Image reconstruction by domain-transform manifold learning. *Nature*, 555(7697):487–492, 2018. doi: 10.1038/nature25988.
- [6] Francesco Tonolini, Jack Radford, Alex Turpin, Daniele Faccio, and Roderick Murray-Smith. Variational inference for computational imaging inverse problems. *Journal of Machine Learning Research*, 21(1):7285–7330, 2020. arXiv:1904.06264 [cs.LG].
- [7] Jonas Adler and Ozan Öktem. Solving ill-posed inverse problems using iterative deep neural networks. *Inverse Problems*, 33(12):124007, 2017. doi: 10.1088/1361-6420/aa9581.
- [8] Ian Goodfellow, Jean Pouget-Abadie, Mehdi Mirza, Bing Xu, David Warde-Farley, Sherjil Ozair, Aaron Courville, and Yoshua Bengio. Generative adversarial networks. In *Advances in Neural Information Processing Systems*, 2014. arXiv:1406.2661 [stat.ML].
- [9] Weihao Xia, Yulun Zhang, Yujiu Yang, Jing-Hao Xue, Bolei Zhou, and Ming-Hsuan Yang. GAN Inversion: A Survey. *IEEE Transactions on Pattern Analysis and Machine Intelligence*, 45(3):3121–3138, 2023. doi: 10.1109/TPAMI.2022.3181070.
- [10] Yang Song and Stefano Ermon. Generative Modeling by Estimating Gradients of the Data Distribution. In *Advances in Neural Information Processing Systems*, 2019. arXiv:1907.05600 [cs.LG].
- [11] Jonathan Ho, Ajay Jain, and Pieter Abbeel. Denoising Diffusion Probabilistic Models. In *Advances in Neural Information Processing Systems*, 2020. arXiv:2006.11239 [cs.LG].
- [12] Alexander Quinn Nichol and Prafulla Dhariwal. Improved Denoising Diffusion Probabilistic Models. In *International Conference on Machine Learning*, 2021. arXiv:2102.09672 [cs.LG].
- [13] Andreas Lugmayr, Martin Danelljan, Andres Romero, Fisher Yu, Radu Timofte, and Luc Van Gool. RePaint: Inpainting Using Denoising Diffusion Probabilistic Models. In *Computer Vision and Pattern Recognition*, 2022. doi: 10.1109/CVPR52688.2022.011117.
- [14] Yang Song and Stefano Ermon. Improved Techniques for Training Score-Based Generative Models. In *Advances in Neural Information Processing Systems*, 2020. arXiv:2006.09011 [cs.LG].
- [15] Yang Song, Jascha Sohl-Dickstein, Diederik P. Kingma, Abhishek Kumar, Stefano Ermon, and Ben Poole. Score-Based Generative Modeling through Stochastic Differential Equations. In *International Conference on Learning Representations*, 2021. arXiv:2011.13456 [cs.LG].
- [16] Yang Song, Liyue Shen, Lei Xing, and Stefano Ermon. Solving Inverse Problems in Medical Imaging with Score-Based Generative Models. In *International Conference on Learning Representations*, 2022. arXiv:2111.08005 [eess.IV].
- [17] Elad Richardson, Yuval Alaluf, Or Patashnik, Yotam Nitzan, Yaniv Azar, Stav Shapiro, and Daniel Cohen-Or. Encoding in Style: A StyleGAN Encoder for Image-to-Image Translation. In *Computer Vision and Pattern Recognition*, 2021. doi: 10.1109/CVPR46437.2021.00232.
- [18] Guim Perarnau, Joost van de Weijer, Bogdan Raducanu, and Jose M. Alvarez. Invertible Conditional GANs for image editing. 2016. arXiv:1611.06355 [cs.CV].
- [19] Rameen Abdal, Yipeng Qin, and Peter Wonka. Image2StyleGAN: How to Embed Images Into the StyleGAN Latent Space? In *International Conference on Computer Vision*, 2019. arXiv:1904.03189 [cs.CV].
- [20] Minyoung Huh, Richard Zhang, Jun-Yan Zhu, Sylvain Paris, and Aaron Hertzmann. Transforming and Projecting Images into Class-Conditional Generative Networks. In *European Conference on Computer Vision*, 2020. doi: 10.1007/978-3-030-58536-5_2.
- [21] Jun-Yan Zhu, Philipp Krähenbühl, Eli Shechtman, and Alexei A. Efros. Generative Visual Manipulation on the Natural Image Manifold. In *European Conference on Computer Vision*, 2016. doi: 10.1007/978-3-319-46454-1_36.

[22] Jiapeng Zhu, Yujun Shen, Deli Zhao, and Bolei Zhou. In-Domain GAN Inversion for Real Image Editing. In *European Conference on Computer Vision*, 2020. doi: 10.1007/978-3-030-58520-4_35.

[23] David Bau, Jun-Yan Zhu, Jonas Wulff, William Peebles, Hendrik Strobelt, Bolei Zhou, and Antonio Torralba. Seeing What a GAN Cannot Generate. In *International Conference on Computer Vision*, 2019. arXiv:1910.11626 [cs.CV].

[24] Jeff Donahue, Philipp Krähenbühl, and Trevor Darrell. Adversarial Feature Learning. In *International Conference on Learning Representations*, 2017. arXiv:1605.09782 [cs.LG].

[25] Vincent Dumoulin, Ishmael Belghazi, Ben Poole, Olivier Mastropietro, Alex Lamb, Martin Arjovsky, and Aaron Courville. Adversarially Learned Inference. In *International Conference on Learning Representations*, 2017. arXiv:1606.00704 [stat.ML].

[26] Jiapeng Zhu, Deli Zhao, Bo Zhang, and Bolei Zhou. Disentangled Inference for GANs With Latently Invertible Autoencoder. *International Journal of Computer Vision*, 130(5):1259–1276, 2022. doi: 10.1007/s11263-022-01598-5.

[27] Giannis Daras, Joseph Dean, Ajil Jalal, and Alexandros G. Dimakis. Intermediate Layer Optimization for Inverse Problems using Deep Generative Models. 2021. arXiv:2102.07364 [cs.LG].

[28] Dmitry Ulyanov, Andrea Vedaldi, and Victor Lempitsky. It Takes (Only) Two: Adversarial Generator-Encoder Networks. In *AAAI Conference on Artificial Intelligence*, 2018. doi: 10.1609/aaai.v32i1.11449.

[29] Varun A. Kelkar and Mark Anastasio. Prior Image-Constrained Reconstruction using Style-Based Generative Models. In *International Conference on Machine Learning*, 2021. arXiv:2102.12525 [eess.IV].

[30] Sachit Menon, Alexandru Damian, Shijia Hu, Nikhil Ravi, and Cynthia Rudin. PULSE: Self-Supervised Photo Upsampling via Latent Space Exploration of Generative Models. In *Computer Vision and Pattern Recognition*, 2020. doi: 10.1109/CVPR42600.2020.00251.

[31] Dmitry Ulyanov, Andrea Vedaldi, and Victor Lempitsky. Deep Image Prior. In *Computer Vision and Pattern Recognition*, 2018. arXiv:1711.10925 [cs.CV].

[32] Olaf Ronneberger, Philipp Fischer, and Thomas Brox. U-Net: Convolutional Networks for Biomedical Image Segmentation. In *Medical Image Computing and Computer-Assisted Intervention*, 2015. doi: 10.1007/978-3-319-24574-4_28.

[33] Reinhard Heckel and Mahdi Soltanolkotabi. Denoising and Regularization via Exploiting the Structural Bias of Convolutional Generators. 2020. arXiv:1910.14634 [cs.LG].

[34] Prithvijit Chakrabarty and Subhransu Maji. The Spectral Bias of the Deep Image Prior. 2019. arXiv:1912.08905 [cs.CV].

[35] Daniel Otero Baguer, Johannes Leuschner, and Maximilian Schmidt. Computed tomography reconstruction using deep image prior and learned reconstruction methods. *Inverse Problems*, 36(9):094004, 2020. doi: 10.1088/1361-6420/aba415.

[36] Piotr Bojanowski, Armand Joulin, David Lopez-Paz, and Arthur Szlam. Optimizing the Latent Space of Generative Networks. In *International Conference on Machine Learning*, 2018. arXiv:1707.05776 [stat.ML].

[37] Idan Azuri and Daphna Weinshall. Generative Latent Implicit Conditional Optimization when Learning from Small Sample. In *International Conference on Pattern Recognition*, 2021. doi: 10.1109/ICPR48806.2021.9413259.

[38] Yedid Hoshen, Ke Li, and Jitendra Malik. Non-Adversarial Image Synthesis With Generative Latent Nearest Neighbors. In *Computer Vision and Pattern Recognition*, 2019. doi: 10.1109/CVPR.2019.00596.

[39] Bi Xiao and Xiaokang Yang. Optimizing Generative Adversarial Networks in Latent Space. In *International Conference on Intelligent Computing, Automation and Systems*, 2019. doi: 10.1109/ICICAS48597.2019.00020.

[40] Frank Natterer and Frank Wübbeling. *Mathematical Methods in Image Reconstruction*. Society for Industrial and Applied Mathematics, 2001. doi: 10.1137/1.9780898718324.

[41] Amir Beck and Marc Teboulle. A Fast Iterative Shrinkage-Thresholding Algorithm for Linear Inverse Problems. *SIAM Journal on Imaging Sciences*, 2(1):183–202, 2009. doi: 10.1137/080716542.

[42] Brian D. O. Anderson. Reverse-time diffusion equation models. *Stochastic Processes and their Applications*, 12(3):313–326, 1982. doi: 10.1016/0304-4149(82)90051-5.

[43] Pascal Vincent. A Connection Between Score Matching and Denoising Autoencoders. *Neural Computation*, 23(7):1661–1674, 2011. doi: 10.1162/NECO_a_00142.

- [44] Alec Radford, Luke Metz, and Soumith Chintala. Unsupervised Representation Learning with Deep Convolutional Generative Adversarial Networks. In *International Conference on Learning Representations*, 2016. arXiv:1511.06434 [cs.LG].
- [45] Diederik P. Kingma and Max Welling. Auto-Encoding Variational Bayes. In *International Conference on Learning Representations*, 2014. arXiv:1312.6114 [stat.ML].
- [46] Lucas Theis, Aäron van den Oord, and Matthias Bethge. A note on the evaluation of generative models. In *International Conference on Learning Representations*, 2016. arXiv:1511.01844 [stat.ML].
- [47] Kenneth Clark, Bruce Vendt, Kirk Smith, John Freymann, Justin Kirby, Paul Koppel, Stephen Moore, Stanley Phillips, David Maffitt, Michael Pringle, Lawrence Tarbox, and Fred Prior. The Cancer Imaging Archive (TCIA): Maintaining and Operating a Public Information Repository. *Journal of Digital Imaging*, 26(6):1045–1057, 2013. doi: 10.1007/s10278-013-9622-7.
- [48] Samuel G. Armato III. The Lung Image Database Consortium (LIDC) and Image Database Resource Initiative (IDRI): A Completed Reference Database of Lung Nodules on CT Scans. *Medical Physics*, 38(2):915–931, 2011. doi: 10.1118/1.3528204.
- [49] Taylor R. Moen, Baiyu Chen, David R. Holmes III, Xinhui Duan, Zhicong Yu, Lifeng Yu, Shuai Leng, Joel G. Fletcher, and Cynthia H. McCollough. Low-dose CT image and projection dataset. *Medical Physics*, 48(2):902–911, 2021. doi: 10.1002/mp.14594.
- [50] Diederik P. Kingma and Jimmy Ba. Adam: A Method for Stochastic Optimization. In *International Conference on Learning Representations*, 2015. arXiv:1412.6980 [cs.LG].
- [51] Samuel L. Smith, Pieter-Jan Kindermans, Chris Ying, and Quoc V. Le. Don’t Decay the Learning Rate, Increase the Batch Size. In *International Conference on Learning Representations*, 2018. arXiv:1711.00489 [cs.LG].